ADVANCED OPTICAL MATERIALS
www.advopticalmat.de

Fiber-Integrated van der Waals Quantum Sensor with an Optimal Cavity Interface

Jong Sung Moon, Benjamin Whitefield, Lesley Spencer, Mehran Kianinia, Madeline Hennessey, Milos Toth, Woong Bae Jeon, Je-Hyung Kim, and Igor Aharonovich**

Integrating quantum materials with fiber optics adds advanced functionalities to a variety of applications, and introduces fiber-based quantum devices such as remote sensors capable of probing multiple physical parameters. However, achieving optimal integration between quantum materials and fibers is challenging, particularly due to difficulties in fabrication of quantum elements with suitable dimensions and an efficient photonic interface to a commercial optical fiber. Here a new modality for a fiber-integrated van der Waals quantum sensor is demonstrated. A hole-based circular Bragg grating cavity from hexagonal boron nitride (hBN) is designed and fabricated, engineer optically active spin defects within the cavity, and integrate the cavity with an optical fiber using a deterministic pattern transfer technique. The fiber-integrated hBN cavity enables efficient excitation and collection of optical signals from spin defects in hBN, thereby enabling all-fiber integrated quantum sensors. Moreover, remote sensing of a ferromagnetic material and of arbitrary magnetic fields is demonstrated. All in all, the hybrid fiber-based quantum sensing platform may pave the way to a new generation of robust, remote, multi-functional quantum sensors.

1. Introduction

Optical fibers underpin many mature technologies ranging from high-speed internet to sensing and imaging. Integrating optical fibers with active functional elements underpins future-generation remote sensing devices, advanced biophotonic and photonic technologies, and enables new modalities for light emitting diodes, lasers and non-linear optics.[1–6] For these reasons, fiber sensors are already used widely in numerous fields, ranging from inertial navigation[7] to medical diagnosis.[8] In the ever-evolving realm of quantum sensing, there is a growing demand for integrating active quantum resources into highly-matured fiber optic platforms. Whilst laser coupling into a fiber is straightforward, achieving efficient excitation and optical readout of an integrated sensor is not, as it requires both mode matching as well as submicron alignment between the functional component (e.g., a quantum emitter) and the fiber.[9,10]

To date, substantial attention has been given to quantum sensors based on the nitrogen-vacancy (NV) center in diamond.[11,12] However, the integration of bulk diamond or nanodiamonds with fibers is challenging for several reasons. First, the NV center emission overlaps spectrally with fiber autofluorescence, which prohibits efficient sensor operation.[13] Second, integration of bulk crystals that possess a high refractive index significantly limits the light extraction efficiency and applications that require nanoscale focusing or spatial resolution.[14] Alternatively, nanodiamonds attached to a fiber core result in inefficient excitation and significant losses at collection pathways, particularly at small numerical apertures (NAs).[10,15] A workaround is to use bulk optics for imaging or integrate nanostructures at the fiber tip, which requires cumbersome manipulation and often results in low

---

J. S. Moon, W. B. Jeon, J.-H. Kim
Department of Physics
Ulsan National Institute of Science and Technology (UNIST)
Ulsan 44919, Republic of Korea
E-mail: jehyungkim@unist.ac.kr

The ORCID identification number(s) for the author(s) of this article can be found under https://doi.org/10.1002/adom.202401987

DOI: 10.1002/adom.202401987

J. S. Moon
Quantum Technology Research Division
Electronics and Telecommunications Research Institute
Daejeon 34129, South Korea

B. Whitefield, L. Spencer, M. Kianinia, M. Hennessey, M. Toth, I. Aharonovich
School of Mathematical and Physical Sciences
University of Technology Sydney
Ultimo, New South Wales 2007, Australia
E-mail: igor.aharonovich@uts.edu.au

B. Whitefield, L. Spencer, M. Kianinia, M. Hennessey, M. Toth, I. Aharonovich
ARC Center of Excellence for Transformative Meta-Optical Systems (TMOS), Faculty of Science
University of Technology Sydney
Ultimo, New South Wales 2007, Australia

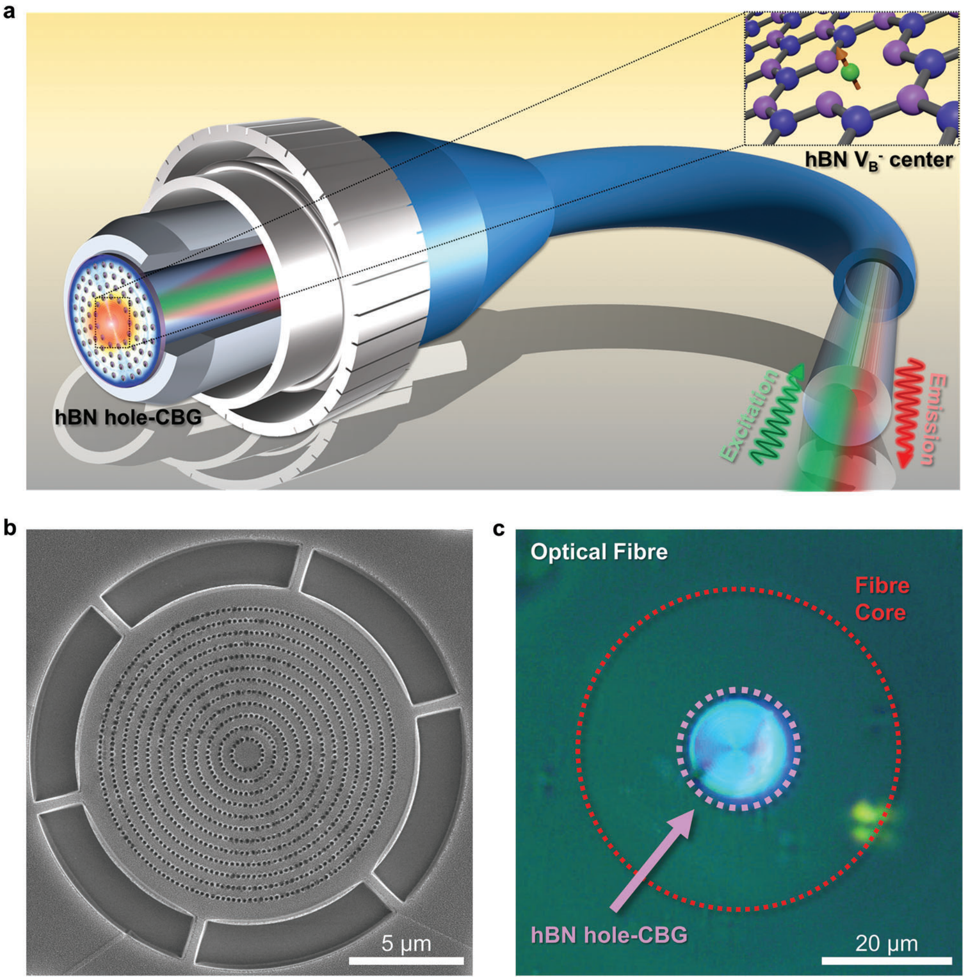

Figure 1. Fiber-integrated quantum sensor a) Schematic illustration of the fiber-integrated quantum sensor. A hBN circular bragg grating (CBG) is placed at the end of the fiber core, enabling excitation and collection of hBN spin defects embedded in the CBG. The inset is a visualisation of the negatively charged boron vacancy, the spin-active defect used for sensing. b) SEM image of the hBN CBG. The CBG is connected to the hBN flake with a sprue-like release structure that is broken when transferring the CBG onto the fiber. c) Optical image of the hBN CBG cavity integrated onto the fiber core.

coupling efficiencies.[16–18] These approaches limit the overall performance and utility of devices and consequently, efficient integration of solid-state quantum sensors and fiber optics has, to date, remained elusive.

The van der Waals material hexagonal boron nitride (hBN) has recently garnered significant attention due to its layered nature and unique optical properties.[19,20] Importantly, it can host on-demand single photon emission, as well as various spin defects that are suitable for quantum sensing applications.[21–27] A major advantage of hBN is the ability to exfoliate thin flakes with controllable thickness, enabling the fabrication of nanophotonic cavities used to enhance light extraction and coupling.[28–30] Additionally, hBN flakes can be positioned easily and deterministically using well-established, mature flake transfer techniques.[31] As a result, hBN is an ideal material platform for hybrid-integrated quantum devices and, particularly appealing for integration with optical fibers.

Here, we introduce a new fiber-integrated hBN cavity, and use it to demonstrate proof-of-principle remote quantum sensing. Specifically, we fabricate a hole-based circular Bragg grating (CBG) cavity that generates a vertically narrow Gaussian beam profile from hBN. We subsequently engineer, on demand, spin defects (negatively charged boron vacancies, V_B^-) within the CBG, and transfer it onto the core of a commercial optical fiber. The engineered fiber cavities overcome the shortfalls of prior attempts by efficiently coupling the emission from V_B^- centers into the fiber, and enable proof-of-principle remote sensing of magnetic fields. Our results constitute a new hybrid system for remote sensing, with unprecedented functionalities.

2. Results and Discussion

Figure 1a schematically illustrates the fiber-integrated quantum sensor consisting of a monolithic CBG hBN cavity integrated with a standard optical fiber. The CBG contains an ensemble of optically-active spin defects that can be excited and read out through the fiber. The inset depicts the V_B^- spin defects in hBN which are used as sensors in this work. The CBG acts both as the cavity for light collection as well as the active medium for quantum sensing. The optical operation, including laser excitation and photoluminescence (PL) collection can all be done through fiber without any additional optical components. See supporting information for cavity fabrication details.

A scanning electron microscopy (SEM) image of a fabricated CBG hBN cavity which is designed to enable ergonomic transfer onto a fiber is shown in Figure 1b. The cavity is composed of a nanohole array that is periodic in both the radial and tangential directions. This design enhances the vertical directionality of the coupled emission compared to a conventional CBG composed of concentric rings.[32] The sprue-like release structure around the CBG provides a temporary mechanical connection to the parent hBN flake – it breaks when the CBG is detached from the flake and transferred to a fiber core. The transfer of the hBN CBG onto the fiber was done using a standard polydimethylsiloxane (PDMS) stamp 2D material transfer technique. Figure 1c shows an optical image of the fiber-integrated CBG device post transfer. Details of the fiber integration process and the cavity fabrication method are described in Supporting Information.

The CBG cavity used in this work was designed specifically to enable integration with a fiber, and to optimise fiber coupling. The design (termed "hole-CBG") replaces the air gaps between the rings of a conventional CBG with nanohole arrays between the rings.[32] This has two primary advantages. First, whilst all CBGs redirect emitted light in a vertical, out of plane direction, the hole-CBG achieves improved narrowing of the emission in the far field, yielding more efficient mode matching and fiber coupling. Second, the entire hole-CBG structure is interconnected structurally, which is critical for robust, reliable transfer of such cavities without geometric distortion and damage that would occur in conventional CBGs comprised of concentric rings separated by continuous air gaps. During CBG fabrication, the supporting sprue-like structures keep the cavity connected to the parent hBN flake until they are broken during the lift-out step of the transfer process. The cavity engineering process is assisted by the layered nature of hBN. First, the ability to exfoliate hBN enables ergonomic fabrication of the thin membranes used to etch CBGs. Second, it simplifies the transfer process, and enables transfer of CBGs onto fiber cores using a low-cost method that is rapid, reliable and can, in the future, be scaled and automated.

To optimize the cavity design, we performed a finite-difference time-domain (FDTD) simulation (See methods). An optimized cavity geometry has the following dimensions: a central disk radius (R) of ≈645 nm, a radial interval between nanoholes arrays (r) of ≈498 nm, a tangential interval between nanoholes (l) of ≈224 nm, and a nanohole radius (a) of ≈75 nm. **Figure** 2a shows the simulated far-field emission profile of the CBG cavity compared to that of a pristine hBN flake. The hBN CBG exhibits a highly-focused beam profile within a propagation angle of 10 degrees, whereas the pristine flake has a widespread emission angle. This simulation confirms that the designed cavities can be efficiently coupled to low-NA optical systems such as optical fibers. To compare the CBG and the pristine hBN flakes quantitatively we calculate, in Figure 2b, the collection efficiency as a function of the numerical aperture. The approximate numerical apertures of single mode fibers, multimode fibers and high-NA optical systems are shaded yellow, green and blue, respectively. In the case of the hBN CBG, 50% collection efficiency can be achieved even at an NA of 0.1, corresponding to a single-mode fiber. A multimode fiber would result in over 80% collection efficiency employing the same CBG cavity. In contrast, emission from pristine hBN is barely coupled to a single mode fiber, and only 20% of the emission is coupled to a multi-mode fiber. The simulations illustrate the high efficiency of the optimized cavity design, and illustrate the ability to interface optimally with optical fibers.

Figure 2c is a simulated mode spectrum of the optimized cavity design. It exhibits an intense, sharp resonance at 850 nm, to maximize the overlap with the V_B- spin defects which have a broad emission at ≈750–900 nm.[23] The cavity mode indicates strong Purcell enhancement (F_P ≈50) which enhances the radiative decay rate of the emitters, and should increase the fluorescence intensity of the defects. We note that the choice of the V_B- spin defect offers a practical advantage in that the emission does not overlap spectrally with the fiber autofluorescence which dominates the red spectral range. Finally, Figure 2d shows the tunability of the cavity mode as a function of the hBN thickness. As anticipated, the cavity mode wavelength red-shifts with increasing thickness of hBN.

Once the parameter space for the hBN cavities was established, the devices were fabricated by patterning the optimized cavity design with e-beam lithography followed by dry etching, and transferred onto optical fibers using a PDMS microstamp. We used a multimode fiber with a core size of 50 µm and NA = 0.22. (See Supporting Information for technical details). First, we characterised the performance of the CBG mounted onto the fiber core **Figure** 3a,b show the FDTD simulation of the near-field power ($|E|^2$) map and the corresponding measured PL map of the hBN CBG cavity, respectively. The emission spectrum in figure 3b was obtained by exciting the hBN CBG with a 532 nm laser using a high NA objective lens and collecting the emission through the fiber. As shown in the two maps, the spatial distribution of the cavity mode is similar to the simulation result, where the strong cavity-enhanced PL is displayed at the center of the CBG cavity. Figure 3c exemplifies the fiber coupling efficiency. We compared the PL emission collected through the fiber from both the integrated hBN CBG, and a pristine hBN flake. The integrated CBG exhibits a significantly enhanced PL emission (x16) relative to that of a pristine hBN flake.

Next, we performed both the excitation and collection of the V_B^- emission from the hBN CBG cavity using the fiber, as is shown schematically in Figure 3d (i.e., without using an objective lens). Further setup details are provided in Supporting Information. A PL spectrum from cavity-coupled V_B^- spin defects is shown in Figure 3e. The distinct sharp peak at 885 nm corresponds to the cavity mode, which dominated the broadband spectrum of the V_B^- emission in the range of 750–900 nm. Thus, we can conclude that the cavity-enhanced V_B^- emissions can be efficiently excited and collected through the optical fiber. Additional measurments are shown in the supporting information.

A key function of the fiber-integrated hBN device is to detect spin-dependent electron transitions of V_B^- defects by monitoring their PL intensity, known as optically detected magnetic resonance (ODMR). Through the application of a resonant radiofrequency (RF) signal, electrons can be cycled between the $|0\rangle$ and $|\pm 1\rangle$ spin states within the electronic ground state manifold Inset in Figure 3f. The resonant frequency of the spin transitions is highly sensitive to external magnetic fields, and thus enables opportunities for high-resolution, high-sensitivity quantum magnetometry.

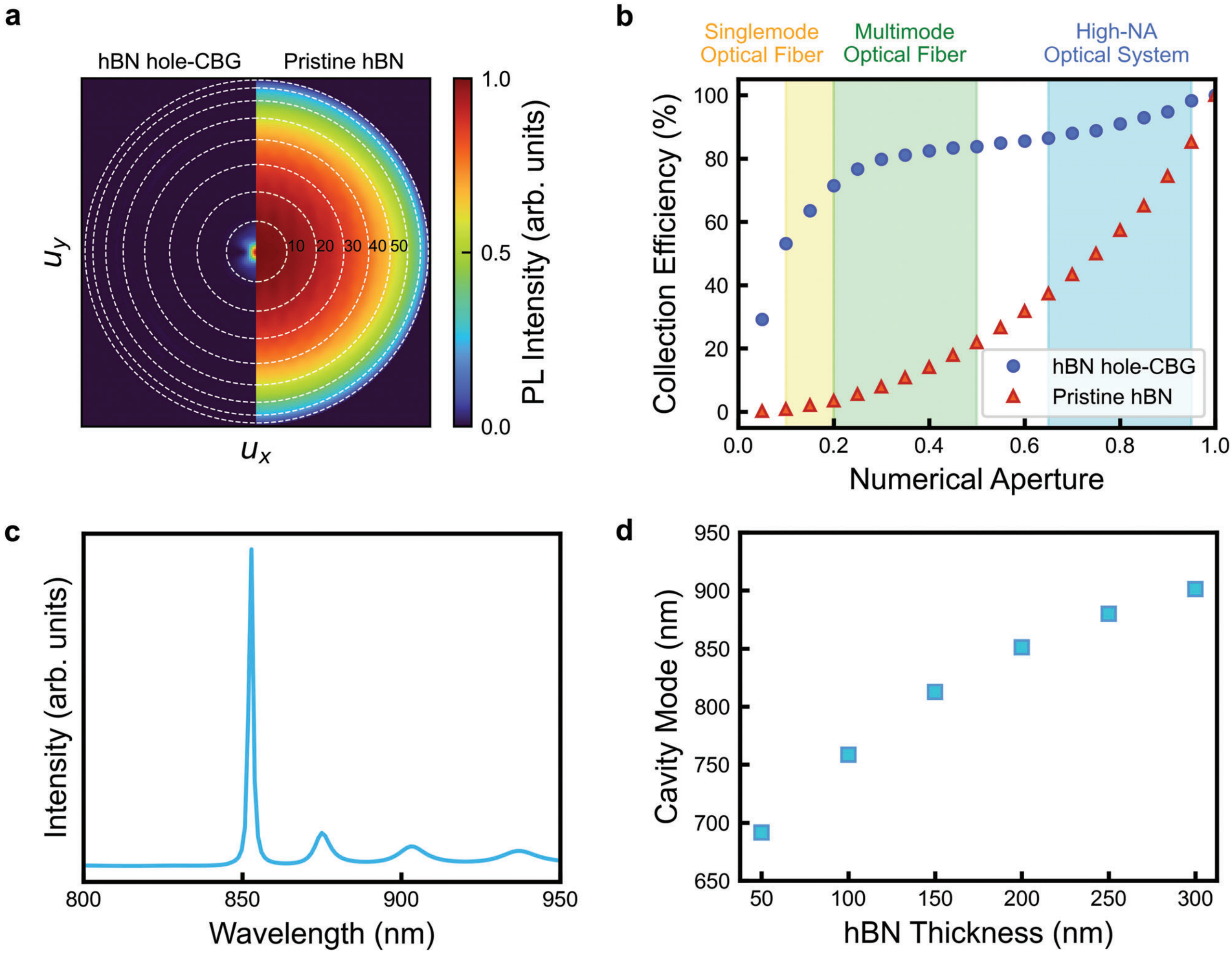

Figure 2. FDTD design of hBN hole-CBG cavities. a) Far-field emission profile map of an optimized hBN hole-CBG (left) and a pristine hBN flake (right) b) Comparison of the collection efficiency of the hBN CBG cavity (blue circles) and a pristine flake of hBN (red triangles) as a function of numerical aperture. The shaded regions (yellow, green, blue) denote the corresponding numerical aperture of a single mode fiber, multimode fiber and a high-NA optical system. c) Simulated cavity mode spectrum in the emission range of the V_B^- defect. d) Central wavelength of the cavity mode as a function of the thickness of the original hBN flake.

We confirmed the sensing functionality by performing ODMR measurements using the fiber-integrated device. The cavity-embedded V_B^- centers were excited and the emission was collected as shown in Figure 3d. An RF antenna was positioned near the fiber as well as an external magnet to induce a weak magnetic field. The ODMR plot is shown in Figure 3f with two distinct transitions at ≈3.3 and ≈3.6 GHz, corresponding to the $|-1\rangle$ and $|+1\rangle$ spin states of the V_B^- defect, respectively. The ODMR contrast is approaching 3%, on par with contrast levels recorded from V_B^- ensembles using bulk optics and confocal microscopes.[33,34] Additional characterization data is shown in the Supporting Information.

The central metric for evaluating the performance of a magnetometer is its sensitivity. The magnetic field sensitivity (η_B) of the fiber-integrated device can be calculated using the following equation:

$$\eta_B\left(T/\sqrt{Hz}\right) = \mathcal{P}_F \times \frac{1}{\gamma_e} \times \frac{\Delta\nu_{lw}}{C\sqrt{R}} \tag{1}$$

where the electron gyromagnetic ratio (γ_e) is equal to 28 MHz mT^{-1} and $\mathcal{P}_F$ is a numerical parameter that is determined by the spin resonance shape, 0.70 for a Gaussian profile (See Supporting Information Section V). The linewidth ($\Delta\nu_{lw}$), ODMR contrast (C) and photon counts per second (R) are all acquired through fitting a Gaussian curve to the ODMR resonant transitions. The calculated magnetic field sensitivity for the fiber-integrated device is $145\ \mu T\ \sqrt{Hz^{-1}}$, which is sufficient for many measurements that require remote sensing, e.g., magnetic particle sensing for drug delivery[35] or electrical current detection.[35] We stress, however, that our CBG-cavity integrated fiber magnetometer is fully mobile, without the necessity of bulk optics, and offers an excellent signal-to-noise ratio due to its operation in the near infrared spectral range.

To demonstrate potential application of the fiber integrated hBN CBG sensor, we used it to detect remotely layers of steel. Nondestructive measurement of metal thickness and uniformity is of great importance in several industrial fields. As is shown schematically in **Figure 4a**, an external magnet was placed above

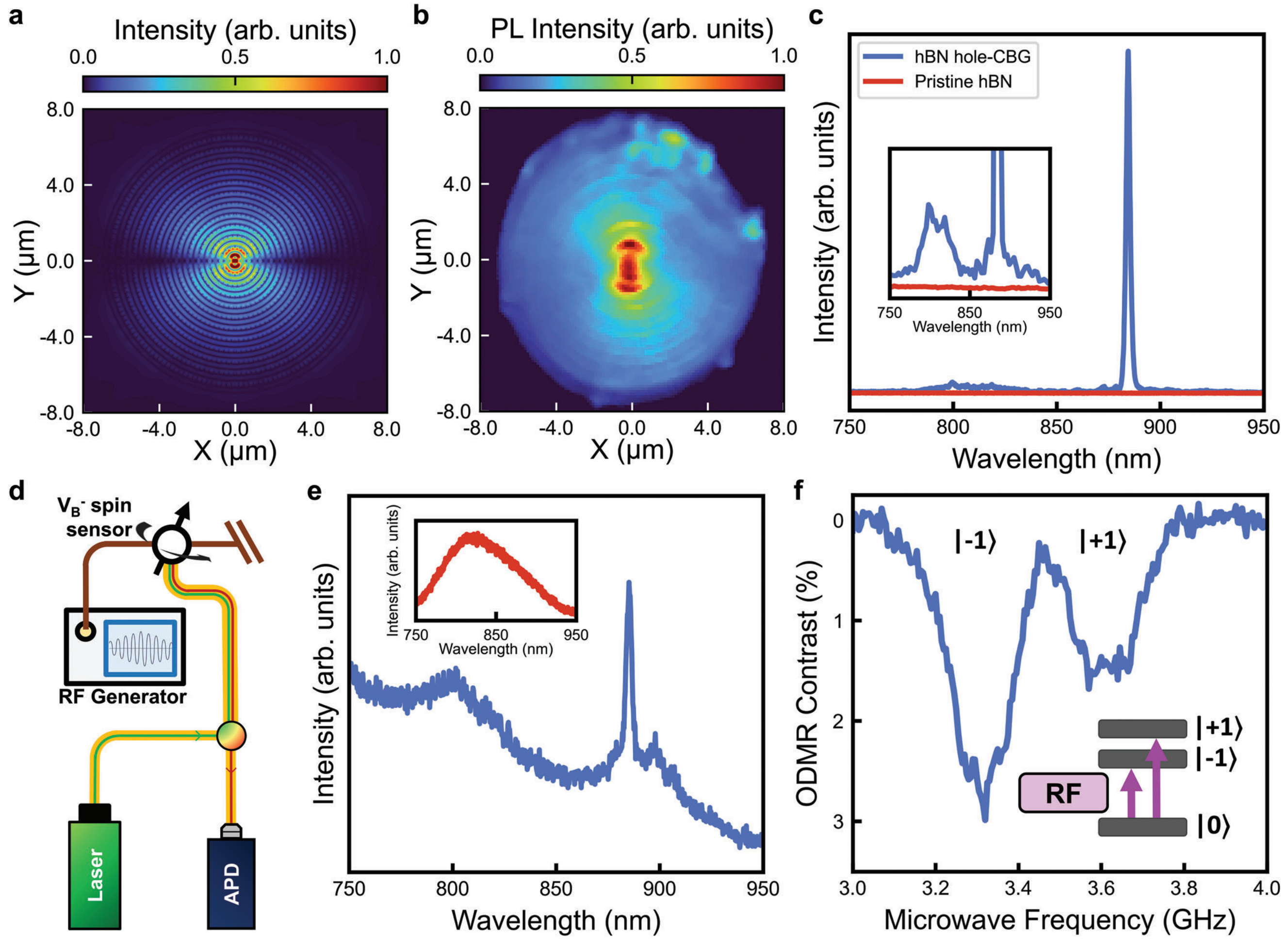

Figure 3. Optical and spin characterization of the fiber-integrated hBN CBG devices. a) FDTD simulation of the near-field power of the hBN CBG cavity, and b) PL map of the fabricated device on an optical fiber excited using a high NA objective and collected through the fiber. The measured spatial distribution of the cavity mode clearly matches the simulation. c) The measured PL spectrum from the integrated hBN CBG cavity (blue) and a pristine hBN flake (red). The excitation and collection setup is similar to (b). The CBG mode can be seen alongside the V_B^- emission in the CBG PL spectrum. The inset is a zoomed-in view of the spectra. d) Simplified schematic of the all-in-fiber excitation and collection configuration. e) PL spectrum obtained using the all-in-fiber configuration of V_B^- defects in the integrated CBG cavity. Inset, V_B^- emission spectrum from non-patterned hBN f) Optically detected magnetic resonance (ODMR) measurement of the integrated hBN CBG cavity. Both excitation and collection are done through the fiber. The inset is a simplified energy level diagram of the V_B^- defect ground state ($S = 1$) split into the three electron spin states: $m_s = 0$, $m_s = \pm 1$.

a sheet of steel of increasing thickness. A fiber tip containing the hBN CBG cavity was brought into proximity of the sample and individual ODMR measurements were recorded. The change in magnetic field strength incident on the fiber modifies the magnitude of Zeeman splitting, and induces a Zeeman shift ($\Delta \boldsymbol{v}_Z$), that maps onto a change in magnetic field strength (B_m) through the following Equation:

$$\Delta\, v_Z = \frac{g_e \mu_B}{h} \cdot B_m \tag{2}$$

Requiring no calibration, the transformation is dictated by two fundamental values, the Bohr magneton (μ_B) and Planck's constant (h), as well as the dimensionless g-factor (g_e), which is approximately equal to 2.0023 for a free electron in a magnetic field. The results of the measurement are shown in Figure 4b along with a representation of the shielding effect observed from wide layers of steel. The two representations refer to the cases with no steel 0 and 9 mm of steel. The optical fiber depicted in the inset indicates where the fiber-integrated CBG was located relative to the magnet and the steel. The change in magnetic field strength due to the increasing thickness of steel was measured by the change in resonant frequency relative to 0 mm of steel (i.e., the strength of the external magnet). Using Equation 2, the change in magnetic field strength due to maximum shielding (9 mm) was calculated to be ≈10.9 mT.

Finally, we present a unique application of the fiber integrated hBN CBG sensor, which measures magnetic field orientation. This functionality relies on the directional uniformity of the V_B^- magnetic dipoles, produced by the D_{3h} symmetry of the defect, which are aligned out of the plane of hBN.[23] In Figure 4c, the external magnetic field was rotated from perpendicular to parallel relative to the hBN plane, while the distance was kept constant.

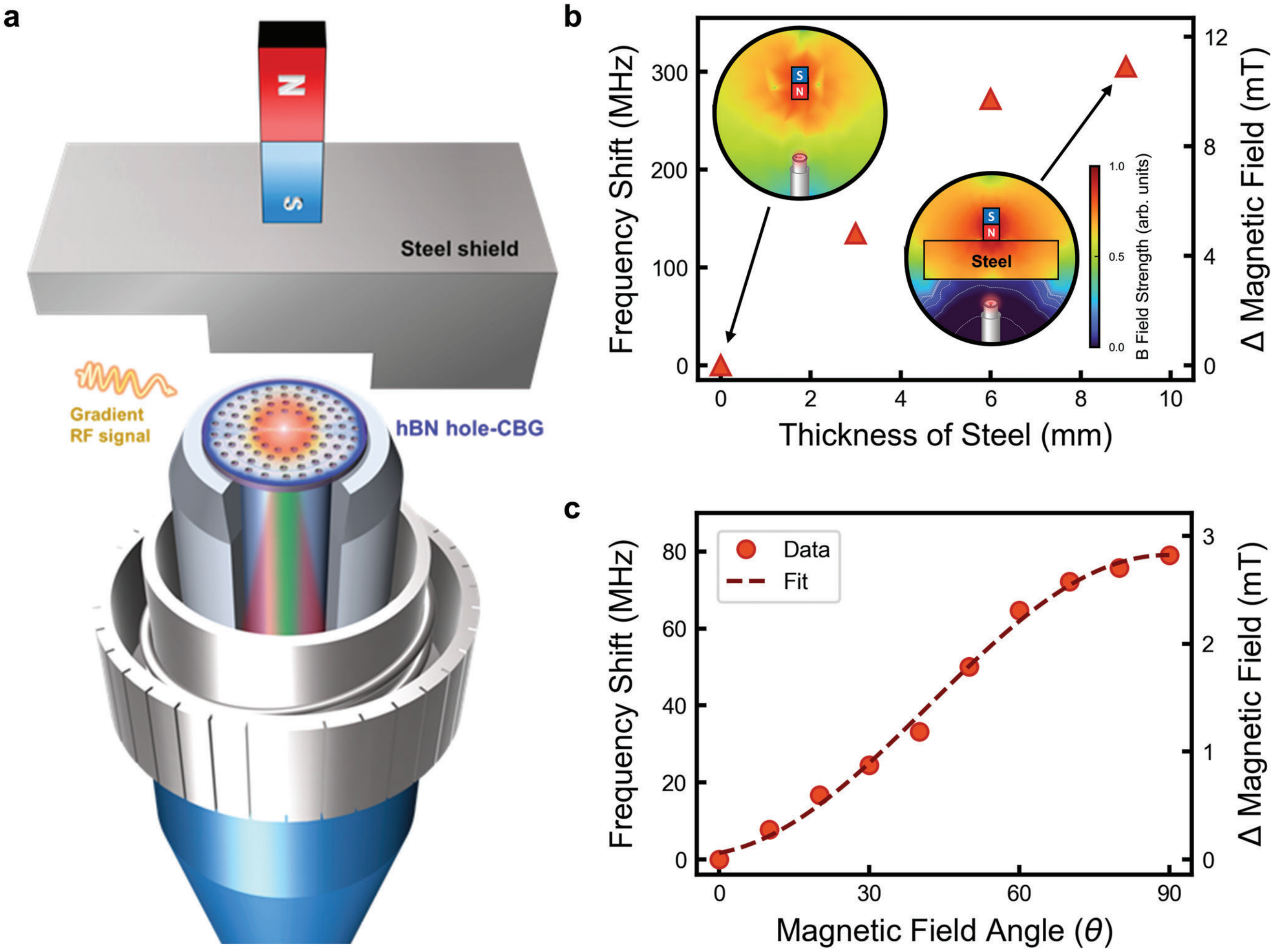

Figure 4. Remote quantum sensing with the integrated hBN CBG fiber. a) Configuration for the remote quantum sensing of increasing layers of steel. b) Plot of change in resonant frequency as a function of steel thickness. The change in magnetic field strength is calculated using Equation 2. The insets show the magnetic field strength incident on the fiber for steel thicknesses of 0 and 9 mm, respectively. c) An external magnet was rotated around the fiber and a change in resonant frequency was recorded. The values are fit with a sinusoidal curve.

The change in magnetic field strength along the V_B^- magnetic dipoles was then measured by the difference in resonant frequency from the perpendicular angle. The strength of the magnetic field vector adheres to a sinusoidal curve and has been fit accordingly. These measurements confirm the successful operation of the fiber-integrated hBN CBG magnetometer without the use of bulk optics.

3. Conclusion

To conclude, we designed and engineered a new generation of fiber-integrated functional sensing devices. In particular, we leveraged the properties of hBN as a van der Waals crystal that hosts optically-active spin defects, to fabricate monolithic CBG cavities, and transferred them onto the core of an optical fiber. We quantified the performance of the sensor by detecting external layers of metal and magnetic field orientation. This remote-sensing technology can be a good alternative to traditional contact-based ultrasound thickness gauges. Possible orientation-sensitive measurements may include imaging in confined spaces and remote locations where bulk optics aren't suitable. Notably, fiber-integrated optically detectable spin states at room temperature offers distinct advantages for imaging liquids, sensing temperature in extreme environments, nondestructively probing molecules, and detecting micro-faults.

Compared to previously demonstrated fiber-integrated sensors, our approach incorporates a nanophotonic cavity with an optimal optical interface. It is advantageous for fiber excitation and collection, as well as enhances the spatial resolution due to its focusing abilities into sub-micron scanning probes, therefore paving ways to achieve super resolution imaging. The demonstrated design and engineering of hBN CBG cavities can also be extended to other applications, facilitating on-demand, room temperature quantum devices. Finally, the approach and the functionality of this method can be extended to other Van der Waals materials such as transition metal di-chalcogenides (TMDCs). While not carrying spin defects, flat lenses from TMDCs can certainly be integrated with fibers,[36] to provide unique opportunities for valley physics.

4. Experimental Section

Fabrication and Design: Finite-difference time-domain (FDTD) simulations were used to optimise nanohole CBG design. The CBG structure was defined by the following four parameters: the radius of the central disk (R), the radial interval between nanoholes arrays (r), the tangential interval between nanoholes (l), and the radius of the nanohole (a). Upon optimisation, the ideal parameters of the cavity design are R ≈645, r ≈498, l ≈224, and a ≈75 nm, designed for an hBN flake with a thickness of 200 nm.

The cavities were patterned using electron beam lithography and transferred into the hBN with fluorine-based reactive ion etching. The hBN flakes were then irradiated with a nitrogen ion beam to create boron vacancies. Devices were then transferred to an etched fiber core with a pattern transfer method using a PDMS stamp. A more in depth fabrication steps could be found in Supporting Information.

Optical Measurements: Objective excitation and fiber collection measurements as seen in Figure 3b,c were performed using a home-built confocal microscope. A 532 nm laser was focused onto the fiber-integrated CBG device by an 100 x (0.9 NA) objective. To obtain the confocal PL image, the fiber-integrated hBN device was scanned using an XYZ piezo stage, and the PL emission was collected through the fiber, and coupled into either a spectrometer or avalanche photodiode (APD). All-in-fiber excitation and collection measurements were completed using the home-built optical setup using a 532 nm laser, coupled into the optical fiber. The emission was collected back through the same fiber. Filtering the laser from the emission was done in a free space, using dichroic mirrors and filters

Optically Detected Magnetic Resonance: ODMR was performed on the fiber-integrated CBG device placing an RF antenna close to the tip of the fiber. A signal generator swept through a range of RF frequencies, and the photons collected by the APD during each signal and reference pulse were then used to calculate the ODMR contrast.

Supporting Information

Supporting Information is available from the Wiley Online Library or from the author.

Acknowledgements

J.S.M., B.W. and L.S. contributed equally to this work. The authors acknowledged financial support from the Australian Research Council (CE200100010, FT220100053, DP240103127), Office of the Naval Research Global (N62909-22-1-2028), the National Research Foundation of Korea grant funded by MSIT (2022M3H4A1A04096396, 2022R1A2C2003176) and the ITRC program (IITP-2023-2020-0-01606, RS-2023-00259676) for financial support. The authors thanks the UTS node of the ANFF for the access to nanofabrication facilities.

Open access publishing facilitated by University of Technology Sydney, as part of the Wiley - University of Technology Sydney agreement via the Council of Australian University Librarians.

Conflict of Interest

The authors declare no conflict of interest.

Data Availability Statement

The data that support the findings of this study are available from the corresponding author upon reasonable request.

Keywords

hBN, quantum sensing, spin defects

Received: July 26, 2024

[1] M. Elsherif, A. E. Salih, M. G. Muñoz, F. Alam, B. AlQattan, D. S. Antonysamy, M. F. Zaki, A. K. Yetisen, S. Park, T. D. Wilkinson, H. Butt, *Advanced Photonics Research* **2022**, *3*, 2100371.

[2] G. Agrawal, In *Nonlinear Fiber Optics*, 5 Edition, Elsevier, Amsterdam, **2012**, pp. 621–629.

[3] C. Jauregui, J. Limpert, A. Tünnermann, *Nat. Photonics* **2013**, *7*, 861.

[4] G. Q. Ngo, E. Najafidehaghani, Z. Gan, S. Khazaee, M. P. Siems, A. George, E. P. Schartner, S. Nolte, H. Ebendorff-Heidepriem, T. Pertsch, A. Tuniz, M. A. Schmidt, U. Peschel, A. Turchanin, F. Eilenberger, *Nat. Photonics* **2022**, *16*, 769.

[5] P. Lu, N. Lalam, M. Badar, B. Liu, B. T. Chorpening, M. P. Buric, P. R. Ohodnicki, *Appl. Phys. Rev.* **2019**, *6*, 041302.

[6] J.-h Chen, Y.-f. Xiong, F. Xu, Y.-q. Lu, *Light: Sci. Appl.* **2021**, *10*, 78.

[7] Z. Wang, G. Wang, S. Kumar, C. Marques, R. Min, X. Li, *IEEE Sens. J.* **2022**, *22*, 18240.

[8] Z. Luo, M. Li, X. Kong, Y. Li, W. Li, Z. Tian, Q. Cao, M. H. Zaman, Y. Li, W. Xiao, Y. Duan, *Interdiscip. Nanomed.* **2023**, *1*, e20230022.

[9] M. Jani, P. Czarnecka, Z. Orzechowska, M. Mrózek, W. Gawlik, A. M. Wojciechowski, *ACS Appl. Nano Mater.* **2023**, *6*, 11077.

[10] Y. Chen, Q. Lin, H. Cheng, H. Huang, J. Shao, Y. Ye, G. S. Liu, L. Chen, Y. Luo, Z. Chen, *ACS Sens.* **2022**, *7*, 3660.

[11] S. C. Scholten, A. J. Healey, I. O. Robertson, G. J. Abrahams, D. A. Broadway, J. P. Tetienne, *J. Appl. Phys.* **2021**, *130*, 150902.

[12] L. Rondin, J. P. Tetienne, T. Hingant, J. F. Roch, P. Maletinsky, V. Jacques, *Rep. Prog. Phys.* **2014**, *77*, 056503.

[13] H. Ebendorff-Heidepriem, Y. Ruan, H. Ji, A. D. Greentree, B. C. Gibson, T. M. Monro, *Opt. Mater. Express* **2014**, *4*, 2608.

[14] F. M. Stürner, A. Brenneis, T. Buck, J. Kassel, R. Rölver, T. Fuchs, A. Savitsky, D. Suter, J. Grimmel, S. Hengesbach, M. Förtsch, K. Nakamura, H. Sumiya, S. Onoda, J. Isoya, F. Jelezko, *Adv. Quantum Technol.* **2021**, *4*, 2000111.

[15] M. Zhao, Q. Lin, Q. Meng, W. Shan, L. Zhu, Y. Chen, T. Liu, L. Zhao, Z. Jiang, *Nanomaterials* **2023**, *13*, 949.

[16] Y. Li, F. A. Gerritsma, S. Kurdi, N. Codreanu, S. Gröblacher, R. Hanson, R. Norte, T. van der Sar, *ACS Photonics* **2023**, *10*, 1859.

[17] R. N. Patel, T. Schröder, N. Wan, L. Li, S. L. Mouradian, E. H. Chen, D. R. Englund, *Light: Sci. Appl.* **2016**, *5*, e16032.

[18] H. Y. Liu, W. Z. Liu, M. Q. Wang, X. Y. Ye, P. Yu, H. Y. Sun, Z. X. Liu, Z. X. Liu, J. W. Zhou, P. F. Wang, F. Z. Shi, Y. Wang, *Adv. Quantum Technol.* **2023**, *6*, 2300127.

[19] S. Vaidya, X. Gao, S. Dikshit, I. Aharonovich, T. Li, *Adv. Phys.: X* **2023**, *8*, 2206049.

[20] J. D. Caldwell, I. Aharonovich, G. Cassabois, J. H. Edgar, B. Gil, D. N. Basov, *Nat. Rev. Mater.* **2019**, *4*, 552.

[21] I. Aharonovich, J. P. Tetienne, M. Toth, *Nano Lett.* **2022**, *22*, 9227.

[22] A. J. Healey, S. C. Scholten, T. Yang, J. A. Scott, G. J. Abrahams, I. O. Robertson, X. F. Hou, Y. F. Guo, S. Rahman, Y. Lu, M. Kianinia, I. Aharonovich, J. P. Tetienne, *Nature Phys* **2022**, *19*, 87.

[23] A. Gottscholl, M. Kianinia, V. Soltamov, S. Orlinskii, G. Mamin, C. Bradac, C. Kasper, K. Krambrock, A. Sperlich, M. Toth, I. Aharonovich, V. Dyakonov, *Nature Mater* **2020**, *19*, 540.

[24] A. Gottscholl, M. Diez, V. Soltamov, C. Kasper, D. Krauße, A. Sperlich, M. Kianinia, C. Bradac, I. Aharonovich, V. Dyakonov, *Nat. Commun.* **2021**, *12*, 4480.

[25] X. Gao, S. Vaidya, K. Li, P. Ju, B. Jiang, Z. Xu, A. E. L. Allcca, K. Shen, T. Taniguchi, K. Watanabe, S. A. Bhave, Y. P. Chen, Y. Ping, T. Li, *Nature Mate* **2022**, *21*, 024.

[26] M. Huang, J. Zhou, D. Chen, H. Lu, N. J. McLaughlin, S. Li, M. Alghamdi, D. Djugba, J. Shi, H. Wang, C. R. Du, *Nat. Commun.* **2022**, *13*, 5369.

[27] K. Sasaki, Y. Nakamura, H. Gu, M. Tsukamoto, S. Nakaharai, T. Iwasaki, K. Watanabe, T. Taniguchi, S. Ogawa, Y. Morita, K. Kobayashi, *Appl. Phys. Lett.* **2023**, *122*, 244003.

[28] J. E. Fröch, L. P. Spencer, M. Kianinia, D. D. Totonjian, M. Nguyen, A. Gottscholl, V. Dyakonov, M. Toth, S. Kim, I. Aharonovich, *Nano Lett.* **2021**, *21*, 6549.

[29] C. Qian, V. Villafañe, M. Schalk, G. V. Astakhov, U. Kentsch, M. Helm, P. Soubelet, N. P. Wilson, R. Rizzato, S. Mohr, A. W. Holleitner, D. B. Bucher, A. V. Stier, J. J. Finley, *Nano Lett.* **2022**, *22*, 5137.

[30] P. Li, I. Dolado, F. J. Alfaro-Mozaz, F. Casanova, L. E. Hueso, S. Liu, J. H. Edgar, A. Y. Nikitin, S. Vélez, R. Hillenbrand, *Science* **2018**, *359*, 892.

[31] A. Castellanos-Gomez, M. Buscema, R. Molenaar, V. Singh, L. Janssen, H. S. J. van der Zant, G. A. Steele, *2D Mater.* **2014**, *1*, 011002.

[32] W. B. Jeon, J. S. Moon, K. Y. Kim, Y. H. Ko, C. J. K. Richardson, E. Waks, J. H. Kim, *Adv. Quantum Technol.* **2022**, *5*, 2200022.

[33] H. Liang, Y. Chen, C. Yang, K. Watanabe, T. Taniguchi, G. Eda, A. A. Bettiol, *Adv. Opt. Mater.* **2023**, *11*, 2201941.

[34] X. Xu, A. B. Solanki, D. Sychev, X. Gao, S. Peana, A. S. Baburin, K. Pagadala, Z. O. Martin, S. N. Chowdhury, Y. P. Chen, T. Taniguchi, K. Watanabe, I. A. Rodionov, A. V. Kildishev, T. Li, P. Upadhyaya, A. Boltasseva, V. M. Shalaev, *Nano Lett.* **2023**, *23*, 25.

[35] D. D. Herea, L. Lăbuşcă, N. Lupu, H. Chiriac, In *Magnetic Sensors and Actuators in Medicine*, (Eds: H. Chiriac, N. Lupu), Elsevier, Amsterdam, **2023**, pp. 259–304.

[36] H. Lin, Z. Q. Xu, G. Cao, Y. Zhang, J. Zhou, Z. Wang, Z. Wan, Z. Liu, K. P. Loh, C. W. Qiu, Q. Bao, B. Jia, *Light Sci Appl* **2020**, *9*, 137.